NANO · MICRO small

www.small-journal.com

Two-Step Synthesis of B_2N_2-Doped Polycyclic Aromatic Hydrocarbon Containing Pentagonal and Heptagonal Rings with Long-Lived Delayed Fluorescence

Huan Luo, Qingyun Wan, Wookjin Choi, Yusuke Tsutsui, Evgenia Dmitrieva, Lili Du, David Lee Phillips, Shu Seki, and Junzhi Liu**

Pentagon–heptagon embedded polycyclic aromatic hydrocarbons (PAHs) have aroused increasing attention in recent years due to their unique physicochemical properties. Here, for the first time, this report demonstrates a facile method for the synthesis of a novel B_2N_2-doped PAH (BN-2) containing two pairs of pentagonal and heptagonal rings in only two steps. In the solid state of BN-2, two different conformations, including saddle-shaped and up-down geometries, are observed. Through a combined spectroscopic and calculation study, the excited-state dynamics of BN-2 is well-investigated in this current work. The resultant pentagon–heptagon embedded B_2N_2-doped BN-2 displays both prompt fluorescence and long-lived delayed fluorescence components at room temperature, with the triplet excited-state lifetime in the microsecond time region ($\tau = 19$ µs). The triplet–triplet annihilation is assigned as the mechanism for the observed long-lived delayed fluorescence. Computational analyses attributed this observation to the small energy separation between the singlet and triplet excited states, facilitating the intersystem crossing (ISC) process which is further validated by the ultrafast spectroscopic measurements.

1. Introduction

Polycyclic aromatic hydrocarbons (PAHs) have attracted great research interest since the pioneering work by Clar and Scholl at the beginning of the 20th century.[1] Since then, various PAHs with different sizes, edge structures, and geometries exhibiting a variety of properties have been designed and synthesized.[2] In addition to typical PAHs with six-membered rings, PAHs with pentagons, such as C_{5v}-symmetric corannulene[3] and C_{3v}-symmetric sumanene,[4] have also been intensively investigated during the past 30 years. In the past decade, heptagon-embedded PAHs have also attracted increasing attention due to their unique curved geometry, which provides an additional pathway to control the optoelectronic properties of PAHs.[5] Very recently, much more effort has been paid to the synthesis of pentagon–heptagon (azulene unit) embedded PAHs.[6] In addition to the incorporation of nonhexagons, the introduction of heteroatoms into the carbon skeleton of PAHs is an effective strategy to modulate their optical and electronic properties, thereby enabling their novel functions.[7] Recently, the implementation of boron–nitrogen (B–N) motifs in PAHs has aroused much interest because of its promising applications in (opto) electronic devices.[8] Compared to the C–C double bonds, the isoelectronic substitution of C=C bonds with B–N units in PAHs impacts the shapes and energies of the highest occupied molecular orbital (HOMO) and/or the lowest unoccupied molecular orbital (LUMO), along with the dipolar moment might generating from the incorporation of B–N units, leading to a significant change in their photophysical properties.[9] In recent years, substantial effort has been dedicated to the synthesis of π-extended PAHs bearing more than one internalized B–N unit, mimicking the structures of classic PAHs with six-membered rings.[10] However, to the best of our knowledge,

H. Luo, Q. Wan, L. Du, D. L. Phillips, J. Liu
Department of Chemistry and State Key Laboratory of Synthetic Chemistry
The University of Hong Kong
Pokfulam Road, Hong Kong 999077, China
E-mail: juliu@hku.hk

The ORCID identification number(s) for the author(s) of this article can be found under https://doi.org/10.1002/smll.202301769.

DOI: 10.1002/smll.202301769

W. Choi, Y. Tsutsui, S. Seki
Department of Molecular Engineering
Graduate School of Engineering
Kyoto University
Nishikyo-ku, Kyoto 615–8510, Japan
E-mail: seki@moleng.kyoto-u.ac.jp

E. Dmitrieva
Leibniz Institute for Solid State and Materials Research (IFW) Dresden
Helmholtzstr. 20, 01069 Dresden, Germany

L. Du
School of Life Sciences
Jiangsu University
Zhenjiang 212013, China

H. Luo
Chemistry and Chemical Engineering Guangdong Laboratory
Shantou 515031, China

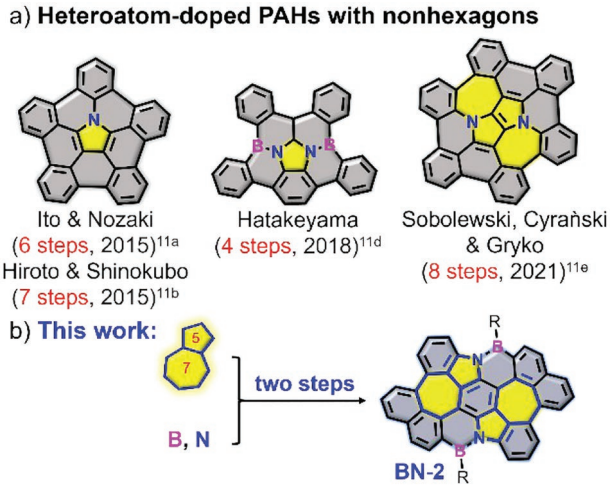

Figure 1. a) Representative examples of heteroatom-doped polycyclic aromatic hydrocarbons (PAHs) with nonhexagons. b) B_2N_2-doped PAH with pentagonal and heptagonal rings reported in this work.

this approach has not been well applied to the synthesis of BN-doped PAHs containing pentagonal and heptagonal rings (**Figure 1**a),[11] apparently due to the challenges of incorporating boron and nitrogen atoms at specific framework positions.

Herein, we report an efficient method for synthesizing a novel B_2N_2-embedded PAH with two pairs of pentagonal and heptagonal rings (**BN-2**, Figure 1b). Compared to the reported heteroatom-doped PAHs with nonhexagons,[11a,11b,11d,11e] which involve multiple synthetic steps (Figure 1a), we develop a large-scale synthesis of **BN-2** in only two steps from commercially available staring materials (**Scheme 1**). Single crystal X-ray analyses unambiguously reveals the unique nonhexagonal topologies embedded in **BN-2**. Interestingly, two different conformations, saddle-shaped and up-down geometries, were found in the solid state of **BN-2** due to steric hindrance among peripheral rings A/B and C/D (**Figure 2**a). The optical property and

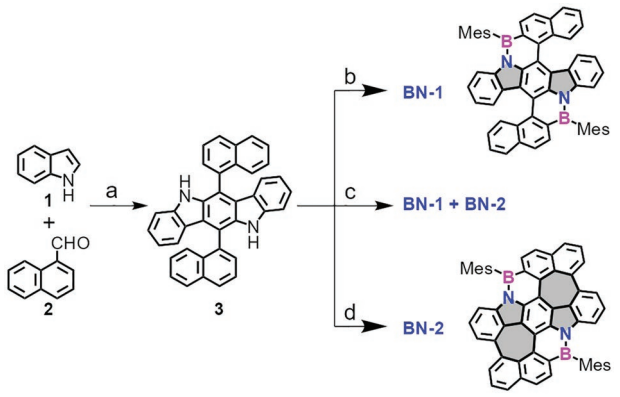

Scheme 1. Synthetic route toward **BN-2**. Reagents and conditions: a) 1) Hydrogen iodide, acetonitrile, 80 °C, 14 h; 2) Pyridinium chlorochromate, ethyl acetate, r.t, 12 h, 40%. b) Boron tribromide, mesitylmagnesium bromide, toluene, 0 °C→110 °C→r.t. **BN-1**: 50%. c) Boron tribromide, aluminum chloride, mesitylmagnesium bromide, toluene, 0 °C→110 °C→r.t. **BN-1**: 20%; **BN-2**: 8%. d) Boron tribromide, aluminum chloride, mesitylmagnesium bromide, *o*-dichlorobenzene, 0 °C→160 °C →r.t. **BN-2**: 20%.

electronic structure of **BN-2** were systematically investigated in this current work using steady-state, time-resolved spectroscopic measurements and density functional theory/temperature-dependent density functional theory (DFT/TDDFT) calculations. The resultant B_2N_2-doped molecule with pentagonal and heptagonal rings (**BN-2**) displayed intense green fluorescence with absolute photoluminescence (PL) quantum yield ($\Phi_{BN\text{-}2}$) of 23.1%. Time-resolved spectroscopies revealed a contribution of long-lived delayed fluorescence in the microsecond time regime to the total fluorescence of **BN-2** (τ = 19 µs), which have not been investigated in other related BN-doped PAHs.[12] Attempts have been made to elucidate the origins of this delayed fluorescence, and the dependence of the delayed fluorescence lifetime on the power of excitation light indicates that triplet–triplet annihilation (TTA) is its most likely mechanism. DFT and TDDFT calculations have revealed a small $\Delta E_{S\text{-}T}$ energy separation (0.01 eV) between the singlet and triplet excited states, leading to a relatively efficient intersystem crossing (ISC) process that could compete with the fluorescence radiative decay. Employing flash-photolysis/field-induced time-resolved microwave conductivity (FP/FI-TRMC) measurements, we demonstrate that **BN-2** possesses an intrinsic charge carrier mobility up to 0.03 $cm^2V^{-1}s^{-1}$, making it a promising material for optoelectronic devices.

2. Results and Discussion

The synthetic route toward compound **BN-2** is described in Scheme 1. First, the key building block 6,12-di(naphthalen-1-yl)-5,11-dihydroindolo[3,2-*b*]carbazole (**3**) was synthesized from the commercially available 1*H*-indole (**1**) and 1-naphthaldehyde (**2**) through condensation and oxidation reactions with a yield of 40%. The borylation of **3** with boron tribromide (BBr_3) followed by workup with mesitylmagnesium bromide (MesMgBr) at room temperature, afforded BN-doped dinaphtho[1,2-*a*:1′,2′-*m*] rubicene with mesityl substituents (**BN-1**) in 50% yield. Interestingly, cyclized BN-doped dinaphtho[1,2-*a*:1′,2′-*m*]rubicene containing two pairs of pentagonal and heptagonal rings (**BN-2**) was also achieved in this one-pot reaction with an isolated yield of 8% in the presence of aluminum chloride ($AlCl_3$). This phenomenon can be ascribed to the synchronous occurrence of the Scholl reaction in the presence of $AlCl_3$, which simultaneously acted as the oxidant and as the Lewis acid. Furthermore, the borylation of **3** led to the only cyclized product (**BN-2**) in a yield up to 20% when the temperature was increased to 160 °C. The chemical structures of **BN-1** and **BN-2** were confirmed by high resolution mass spectrometry (HR-MS) and nuclear magnetic resonance (NMR) analyses (see the Supporting Information).

Single crystals of **BN-2** were grown by slow evaporation from an *n*-hexane/carbon disulfide solution. Interestingly, in the solid state of **BN-2**, there are two different conformations because of the steric hindrance among peripheral rings A–D (Figure 2a), which is quite a rare phenomenon for PAHs. The four peripheral rings A–D adopt an up-down–down-up conformation (up–down geometry) and an up-down–up-down conformation (saddle-shaped geometry) with a ratio of 1:1 in the crystal, in which the distortion angle of the up-down geometry (25.1°) is much smaller than that of the saddle-shaped geometry (31.5°). The

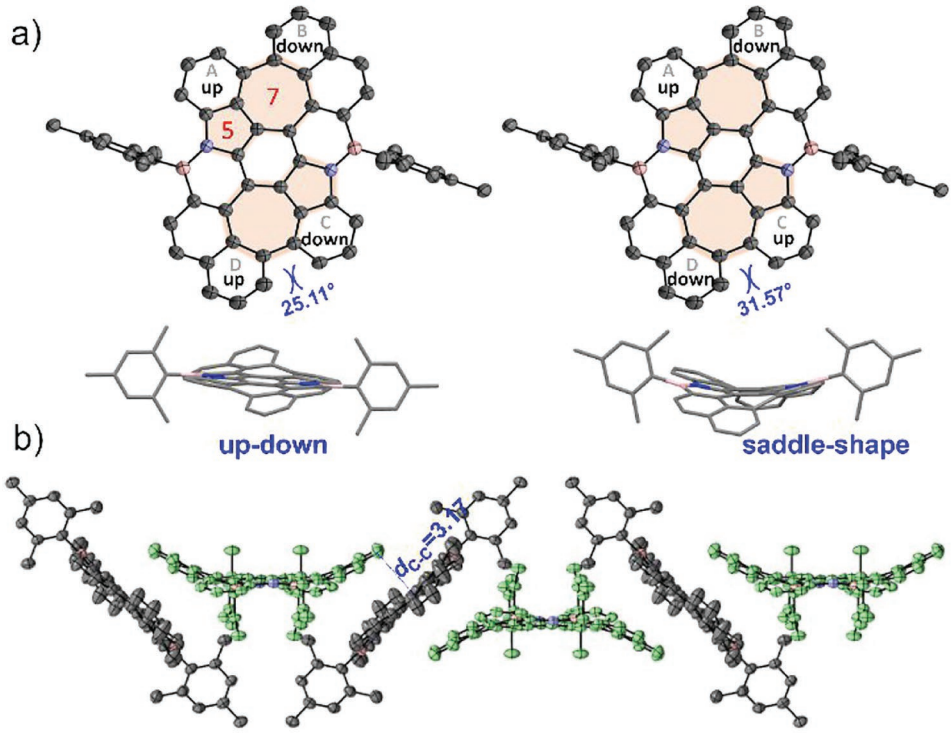

Figure 2. X-ray crystallographic molecular structure. a) Top and side views of **BN-2**. b) Crystal packing of **BN-2**; gray: up-down geometry; light green: saddle-shaped geometry. The hydrogen atoms are omitted for clarity.

B–N bond length in **BN-2** (1.41 Å) is much shorter than a typical B–N single bond (1.58 Å), demonstrating typical delocalized B=N double bonds. In the packing pattern, **BN-2** crystallizes along the *a*-axis of the unit cell with a pair of up-down and saddle-shaped conformations to form one-dimensional chain alignments with a short C···C distance of 3.17 Å (Figure 2b).

Figure 3a shows the absorption and emission spectra of compounds **BN-1** and **BN-2** in dichloromethane (CH_2Cl_2). Vibronic structured absorption bands ranging from 400 to 500 nm are observed for **BN-1** and **BN-2**, which are ascribed to π–π^* transitions in nature. Upon increasing the π conjugation from **BN-1** to **BN-2**, the lowest-energy absorption bands redshifted from 464 to 486 nm. This observation pertains to the delocalization characteristics of the π–π^* transitions in these BN-doped PAHs. A more π-extended conjugation in **BN-2**, versus **BN-1**, leads to a narrower HOMO-LUMO gap and redshifted absorption bands. Small Stokes shifts of 0.07 eV and 0.05 eV are observed for the **BN-1** and **BN-2**, respectively, reflecting a relative small structural distortion upon the emission process. The smaller Stokes shift of 0.05 eV in compound **BN-2** indicates that the cyclized BN-doped compound with pentagonal and heptagonal rings has a more rigid structure than **BN-1**, leading to less structural distortion upon photoexcitation and emission processes. The rigid structure of **BN-2** was further confirmed by the reorganization energy simulations based on DFT/TDDFT calculation, in which the values of **BN-1** and **BN-2** were estimated to be 3.92 kcal mol^{-1} and 2.61 kcal mol^{-1}, respectively. Vibronic emission bands are observed, with 0–0 emission peak maxima of 477 and 496 nm recorded for **BN-1** and **BN-2**, respectively. Relatively high emission quantum yields of 32.3% and 23.1% are observed in compounds **BN-1** and **BN-2**. Compared with **BN-1**, the low quantum yield of **BN-2** is likely owing to the greater intermolecular π–π stacking interactions resulting from its planar structure.[12c] The electrochemical properties of **BN-1** and **BN-2** were then investigated by cyclic voltammetry (CV) in a dichloromethane solution (Figure 3b). **BN-1** exhibits an obvious irreversible oxidation wave with a peak maximum at 0.95 V versus ferrocene/ferrocene$^+$ (Fc/Fc^+) indicating that the electrochemical reaction is followed by a fast follow-up chemical one. In the further cycles, a reversible redox event appears at the potential of 0.38 V and the current intensity increases with increasing of cycle number (Figure S15, Supporting Information). The CV of the compound **BN-2** shows a reversible oxidation at half-wave potential of 0.69 V. The shift of the oxidation potential to more negative value together with the reversible redox behavior of **BN-2** indicates the formation of a stable radical cation due to a larger π-conjugation in the molecule compared with **BN-1**. When the potential sweep is extended to more positive values including the irreversible process with a peak at 1.15 V, additional redox couples at 0.15 V and 0.81 V are observed in the CV of **BN-2**. Additional reversible events at low potential in the cyclic voltammogram of **BN-1** and **BN-2** points to the formation of the electrochemically active products.

The reversible redox behavior of **BN-2** enables their detailed characterization by in situ electron paramagnetic resonance (EPR) and UV–Vis–near infrared (UV–Vis–NIR) absorption spectroscopy. The spectroelectrochemical results are displayed in Figure 3c,d. Upon oxidation, an unresolved EPR signal with a *g*-value of 2.0026 and UV–Vis–NIR absorption bands

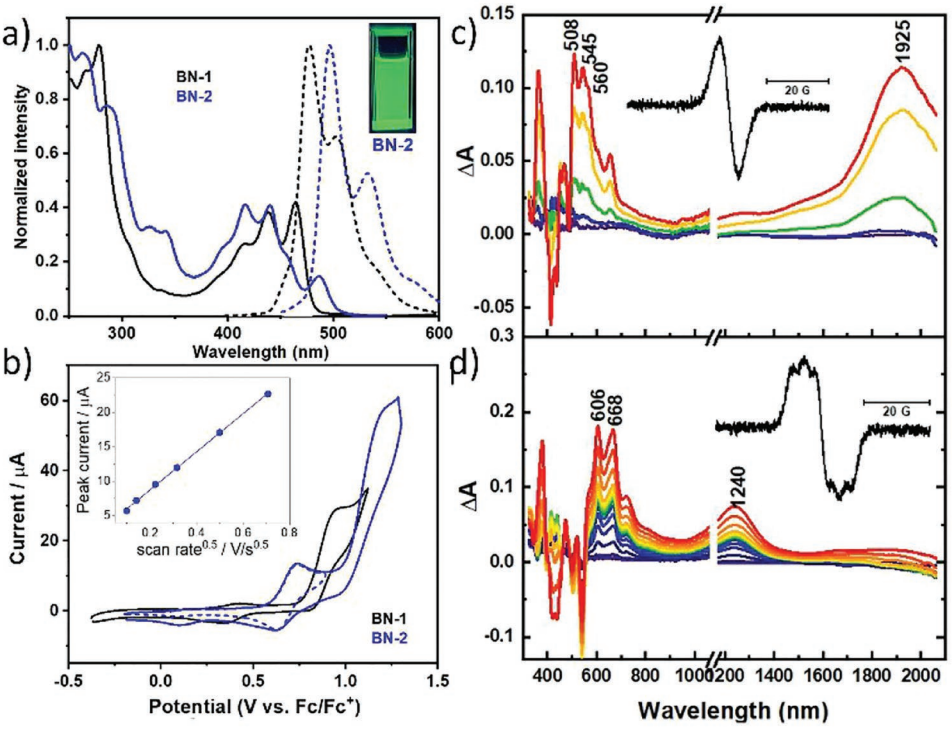

Figure 3. a) Absorption (solid line) and emission (short dash line) spectra of **BN-1** and **BN-2** in CH_2Cl_2 at room temperature (insert: photograph of **BN-2** under 254 nm UV light). b) Cyclic voltammogram of **BN-1** and **BN-2** measured on platinum(Pt) in CH_2Cl_2 (0.1 M *n*-$BuNPF_6$) at the scan rate of 0.1 V s^{-1}. Inset: dependence of the anodic peak current (reversible process) on the square root of the scan rate. In situ UV–Vis–NIR and electron paramagnetic resonance (EPR) (inset) spectra measured in CH_2Cl_2 (0.1 M *n*-$BuNPF_6$) during the oxidation of **BN-2** in the first (c) and third (d) voltammetric cycle. The potential values increase from violet to red.

at 508, 545, 560 and 1925 nm appeared at ≈0.7 V (Figure 3c). The spectroscopic features show the same dependence on the applied potential (Figure S16, Supporting Information). These features can be attributed to a radical cation **BN-2**•+. The occurrence of a broad signal without hyperfine splitting reveals that the spin density in radical structure is distributed over the whole molecule. In the backward potential scan, a new five-line EPR signal with a *g*-value of 2.0029 was detected. The hyperfine structure caused by two equivalent nitrogen nuclei ($a(^{14}N)$ = 3.7 G) points that the spin in the second radical is rather localized. The UV–Vis–NIR absorption spectra show additional bands at 606, 668 and 1240 nm. In the consecutive voltammetric cycles, the spectroscopic features (both EPR and UV–Vis–NIR) of the second radical specie are visible at lower potential (≈0.1 V) and dominate in the spectra (Figure 3d). The spectroelectrochemical experiments prove the formation of the radical monocharged radical species of **BN-2** as well as the oxidation product(s) as result of a follow-up chemical reaction.

Nanosecond time-resolved emission (ns-TRE) spectra of **BN-1** (**Figure 4**a) and **BN-2** (Figure 4b) in deaerated CH_2Cl_2 solution were measured at different time delays. A long-lived emission species with the lifetime in the microsecond time region was probed for these BN-doped PAHs by ns-TRE (τ = 14 and 19 μs for **BN-1** and **BN-2**, respectively) at room temperature. Two emission components are observed at different time delays, including a major component that decays within nanoseconds and a minor component with a microsecond decay lifetime (Figure S2, Supporting Information). These two decay components have identical emission profiles and peak energies. Therefore, the short-lived and long-lived fluorescence are assigned to prompt fluorescence and delayed fluorescence, respectively. The proportion of the delayed fluorescence and prompt fluorescence of **BN-1** and **BN-2** were estimated by integrating the emission intensity over time ranges of 0–50 ns and 50 ns–50 μs, respectively (Figure S2, Supporting Information). The proportion of the delayed fluorescence is 2.7% and 12.1% for **BN-1** and **BN-2**, and their according prompt fluorescence is recorded to be 97.3% (**BN-1**) and 87.9% (**BN-2**), in which the pentagon–heptagon embedded **BN-2** possesses a larger proportion of the delayed fluorescence. The mechanism of the delayed fluorescence could be inferred from the dependence of the delayed fluorescence lifetime on the power of excitation light, with lower pump intensities leading to longer delayed fluorescence lifetimes (Figure S1, Supporting Information). This indicates that exciton–exciton annihilation[13] plays a significant role during the delayed fluorescence process, and that TTA is the likely mechanism (vide infra).

Long-lived excited-state species of **BN-1** (Figure 4c) and **BN-2** (Figure 4d) were similarly investigated using nanosecond transient absorption (ns-TA) spectroscopy at different time delays. These complexes display ground-state bleaching (GSB) in the range of 400–500 nm and a broad positive excited-state absorption (ESA) band ranging from approximately 500 to 700 nm. These signals in the microsecond time regime are indicative of

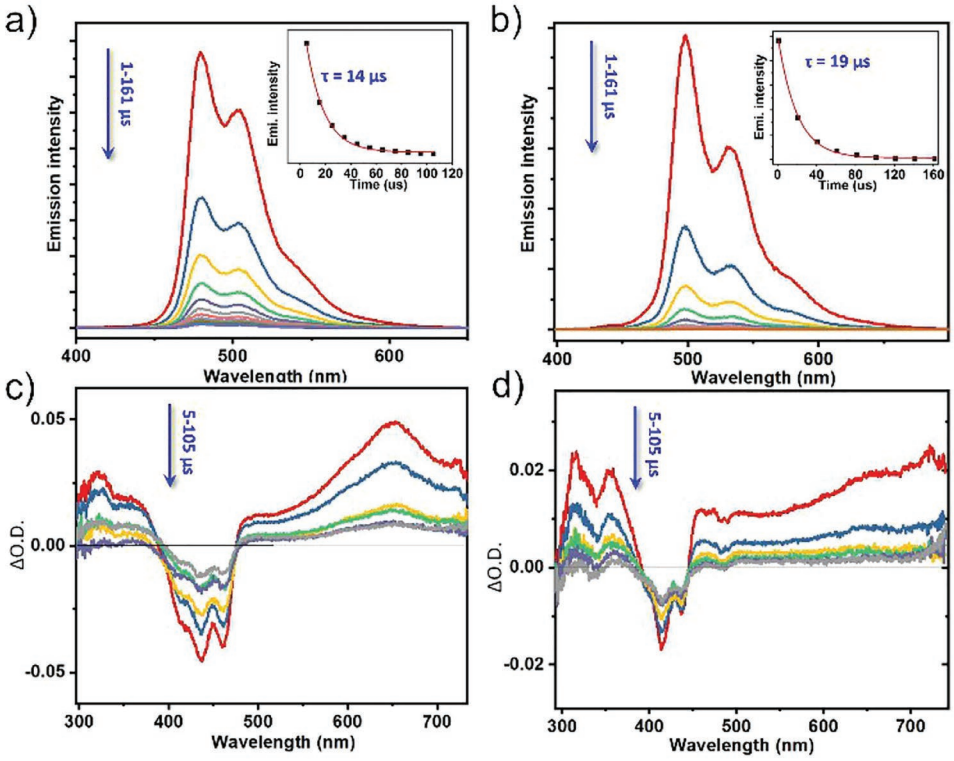

Figure 4. ns-TRE spectra of **BN-1** (a) and **BN-2** (b) in deaerated CH_2Cl_2 solution recorded from 1–161 μs at 298 K. Inset is the emission kinetic decay trace. Decay time constants were fitted as monoexponential decay (λ_{ex} = 355 nm). ns-TA difference spectra of **BN-1** (c) and **BN-2** (d) recorded from 5 to 105 μs at 298 K in deaerated CH_2Cl_2.

a long-lived excited state species and are assigned to the triplet excited state of these BN-doped aromatics.

The femtosecond time-resolved absorption difference (fs-ta) spectra of **BN-1** and **BN-2** obtained immediately after laser pulse excitation at 355 nm revealed an absorption difference peak maxima at ≈600 nm for **BN-1** and ≈570 nm for **BN-2**, respectively (**Figure 5**a,d). The spectral profiles showed a time constant of 12.6 ps for **BN-1** (Figure 5b,c) and 2.0 ps for **BN-2** (Figure 5e,f), which is ascribed to an ISC process. As revealed by the DFT and TDDFT calculations (vide infra), the relative fast ISC process in **BN-2** (2.0 ps) compared to **BN-1** (12.6 ps) is due to a small energy separation between the singlet excited state and triplet excited state of **BN-2**.

DFT/TDDFT calculations were performed on compounds **BN-1** and **BN-2** to gain insight into the nature of their excited states and the mechanism behind the long-lived delayed fluorescence observed as a result of their triplet excited states. As shown in Figure S17 (Supporting Information), the calculated highest-energy absorption bands of **BN-1** and **BN-2** are located at 2.71 and 2.51 eV, respectively, which are consistent with the experimental observation (λ_{expt} = 2.67 and 2.55 eV for **BN-1** and **BN-2**, Figure 3a). Vibrationally resolved emission spectrum was simulated for **BN-2** based on its optimized S_1 structure (Figure S18, Supporting Information). The calculated emission spectrum exhibits emission peaks at 2.31, 2.14 and 1.95 eV (sh), which are consistent with the experimental findings of 2.50, 2.32, 2.13 eV (sh), respectively. The energy difference between these vibrationally resolved emission bands is 0.18 and 0.19 eV by experimental observations, and 0.17 and 0.19 eV by calculations (Figure S18, Supporting Information). These results lend support to the reliability of the Frank–Condon factor calculations used in this work. To account for the observed small Stokes shift in **BN-2**, Huang–Rhys factor was calculated for the $S_1 \rightarrow S_0$ transition of **BN-2** and the results are shown in Figures S19–S21 (Supporting Information). The calculated largest Huang–Rhys factor of **BN-2** is contributed by vibrational mode 13, which is 0.11. The relatively small Huang–Rhys factor in **BN-2** is considered to lead to slow nonradiative decay rate and small Stokes shift. As shown in **Figure 6**a, the S_1 state of **BN-2** is mainly from a mixed transition of HOMO→LUMO and HOMO→LUMO+1. The T_1 state of **BN-2** is mainly from the HOMO→LUMO transition. A delocalized $^{1/3}[\pi\text{–}\pi^*]$ transition is assigned to the S_1 and T_1 excited states of **BN-2** (Figure 6a).

Relatively large proportion of the delayed fluorescence (≈12.1%) was observed in pentagon–heptagon embedded **BN-2** by ns-TRE. Mechanism of the ISC and TTA process in **BN-2** was investigated by calculations. The energies of the singlet and triplet excited states for **BN-2** at the respective optimized S_1 and T_1 geometries are displayed in Figure 6b. Five triplet excited states (T_1-T_5) lie lower than S_1, and the closest-lying T_5 excited state is only 0.01 eV below the S_1 state. Thus, we conclude that the thermal energy at room temperature would assist a relatively facile ISC process of **BN-2**.[14] Figure 6c shows the proposed mechanism of the TTA process occurring in **BN-2**: a facial ISC process is proposed to occur because of the small energy difference between the S_1 and T_5 excited states, after

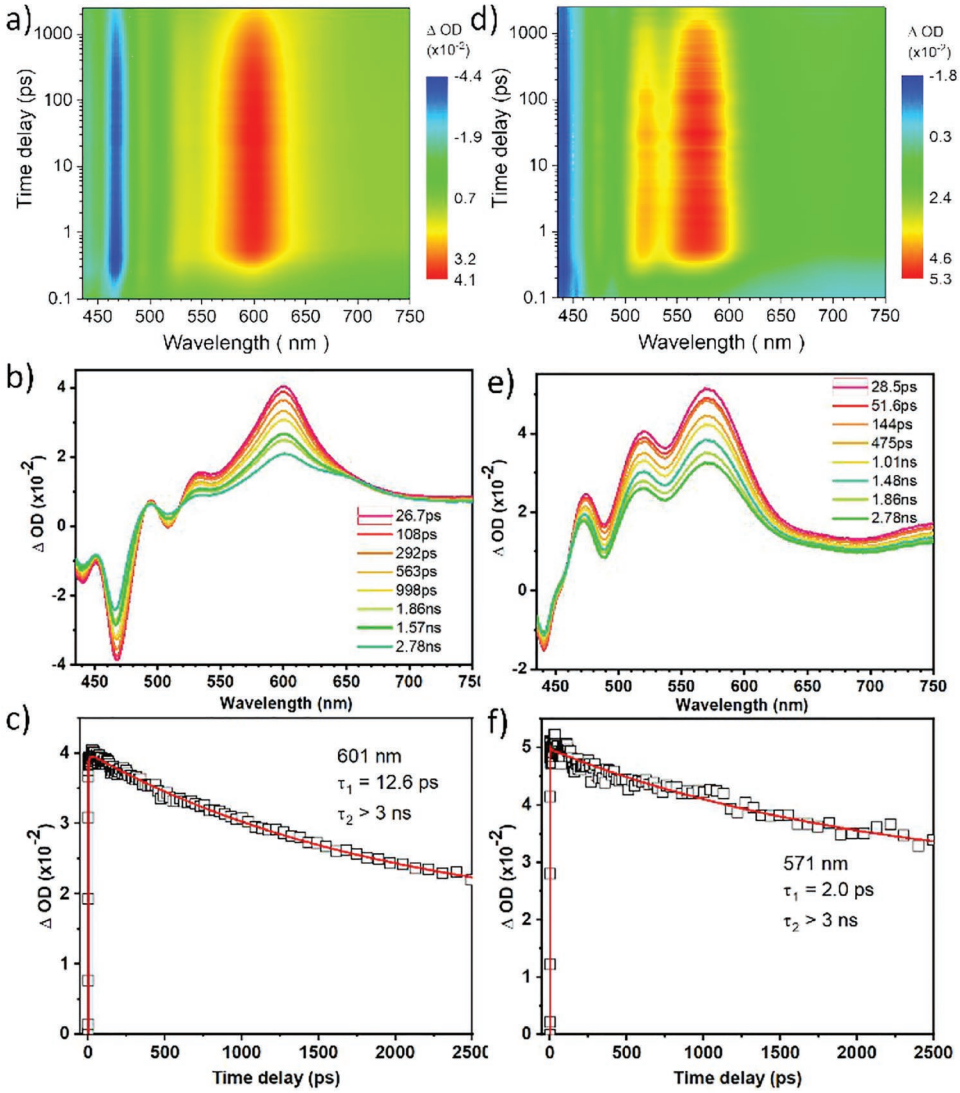

Figure 5. Femtosecond transient absorption spectra for **BN-1** (a–c) and **BN-2** (d–f) in CH_2Cl_2 at various delay times.

which an internal conversion from the T_5 to the T_1 excited state occurs. The annihilation between two T_1 excited states would lead to the generation of an S_1 excited state and an S_0 ground state of **BN-2**. The radiative decay of the $S_1 \rightarrow S_0$ transition generates delayed fluorescence with a microsecond lifetime. The calculated thermodynamic driving force for TTA in **BN-2**, $2 \times E(T_1)–E(S_1)$, is 0.53 eV.[15]

One dimensional chain alignment with the short intermolecular contacts of 3.17 Å in crystalline **BN-2** (Figure 2b) motivated us to examine charge transport properties along the chain directions. The low oxidation potential as well plausible TTA processes upon exposure to 355 nm secures photogeneration of charge carriers though the major energy dissipation pathways are delayed fluorescence via direct transition. Flash-photolysis time-resolved microwave conductivity (FP-TRMC) measurements were then employed to measure the intracrystalline domain electric conductivity of photogenerated charge carriers.[16] The observed photoconductivity transients were shown in **Figure 7**a for vacuum deposited films of both **BN-1** and **BN-2**. **BN-2** gave a considerable photoconductivity transient, which was contrasting to the negligible conductivity transient recorded in **BN-1**. It should be noted that the rapid degradation of the transient observed upon exposure to 355 nm with the significantly high photon density of $>1 \times 10^{16}$ photons cm^{-2} (Figure 7b). This is consistent with the irreversibility of the first oxidation potential in CV of the compounds; the conducting pathways even in crystalline phase of **BN-2** disrupt by the reactions mediated by photogenerated radical cations: the major charge carriers. To minimize the effects of TTA processes (and subsequent photochemical reactions) in charge transport assessments, field-induced time resolved microwave conductivity (FI-TRMC) measurements were then used to estimate the mobility at the interfaces without photoexcitation. Metal–insulator–semiconductor (MIS) structure of the compounds was fabricated with **BN-1** and **BN-2**,[17] respectively, as semiconductor layers, and the charge carriers were injected at the semiconductor–insulator boundary. The correlation is represented in Figure 7c,d (Figure S3, Supporting Information)

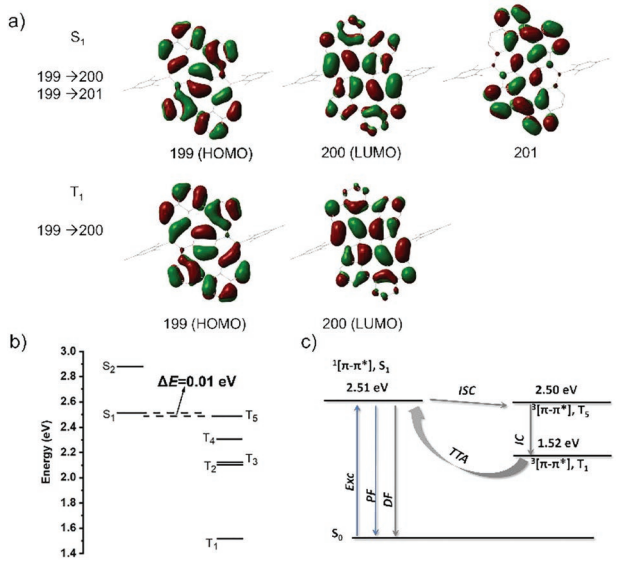

Figure 6. a) The frontier molecular orbitals of **BN-2** accounting for $S_1 \rightarrow S_0$ and $T_1 \rightarrow S_0$ transitions. b) Illustration of the low-lying singlet and triplet excited states of **BN-2**. c) A scheme illustrating the TTA process in **BN-2**. Exc: excitation. IC: internal conversion. PF: prompt fluorescence. DF: delayed fluorescence.

between the interfacial electric conductivity and the number of charge carriers accumulated. Significant slopes were seen only in case of negative bias applied to the MIS structures of both **BN-1** and **BN-2**, suggesting the major charge carriers are positive holes accumulated at the interfaces. The slopes in the figure directly deliver the local mobility of holes in the compounds, leading to the estimates of 0.006 $cm^2V^{-1}s^{-1}$ in **BN-1** and 0.03 $cm^2V^{-1}s^{-1}$ in **BN-2**, respectively. Topographic images of corresponding films show the larger crystalline domains than 100 nm (Figure S4, Supporting Information), securing that both FP- and FI-TRMC measurements are probing intradomain charge carrier mobility. The 1D chain like structures have been realized in the crystalline packing of **BN-2** (Figure 2b) contributing to as the moderate charge transporting pathways, however the close contacts between the adjacent planar **BN-2** molecules are hampered by the Mes groups; this is the case giving the not remarkably high mobility in the regime of charge carrier hopping.

3. Conclusion

In summary, we have demonstrated an efficient strategy for synthesizing a novel B_2N_2-doped PAH with two pairs of pentagonal and heptagonal rings in only two steps. The solid-state structure of **BN-2** contains two different conformations (saddle-shaped and up-down geometries) due to steric hindrance among the peripheral rings. ns-TRE and ns/fs-TA measurements reveal that this pentagon–heptagon embedded **BN-2** displayed both prompt fluorescence and long-lived delayed fluorescence components, with triplet excited-state lifetimes in the microsecond

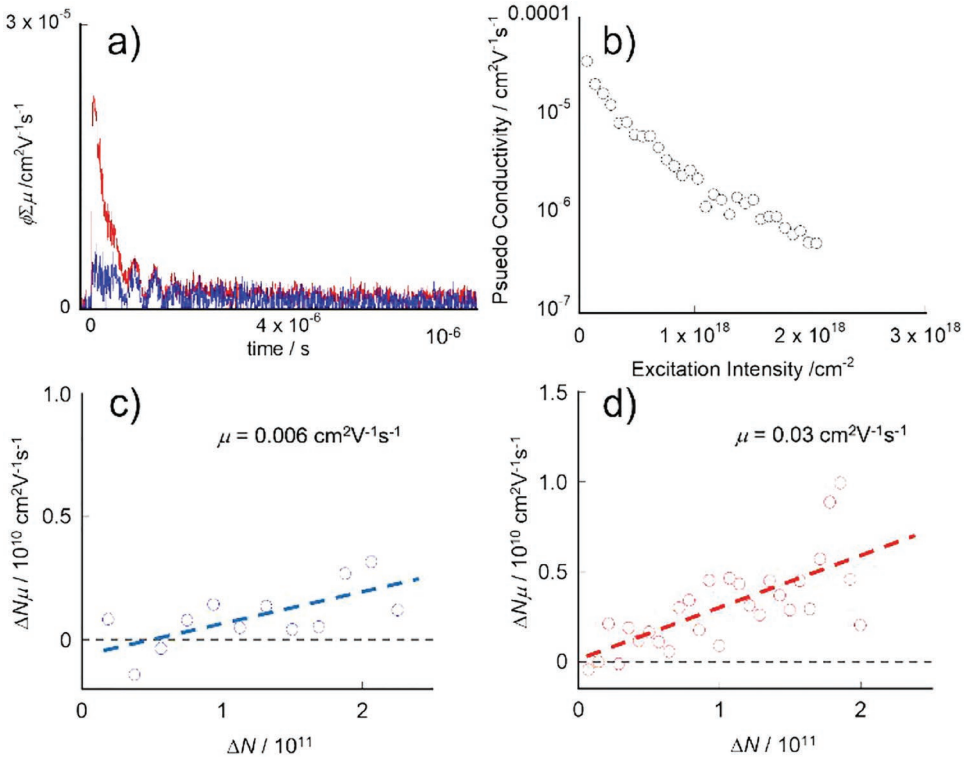

Figure 7. a) Photoconductivity transients observed in vacuum-deposited polycrystalline **BN-1**(blue) and **BN-2** (red) films upon exposure to 355 nm at 2.7×10^{16} photons cm^{-2}. The transients were averaged over 5 pulses irradiated. b) Dependence of maximum photoconductivity recorded in an identical film of **BN-2** upon continuous exposure to 355 nm on integrated photon density. c,d) Correlation between the pseudo microwave conductivity, $N\mu$, and the number of the injected carrier, ΔN, for c) **BN-1** and d) **BN-2**.

time region. This interpretation is supported by DFT/TDDFT calculations, suggesting that TTA is the most likely mechanism for the observed delayed fluorescence. Employing FI-TRMC measurements, the local mobility of holes in **BN-2** is estimated to be 0.03 $cm^2V^{-1}s^{-1}$, demonstrating the promising feature of **BN-2** as n-type semiconducting organic materials. This work provides new application perspectives for PAHs with pentagonal and heptagonal rings and for the design of new materials with enhanced properties for organic electronics.

Supporting Information

Supporting Information is available from the Wiley Online Library or from the author.

Acknowledgements

This work was supported by the Hong Kong Research Grants Council (27301720, 17304021), National Natural Science Foundation of China (22122114), and in part supported by a Grant–in–Aid for Transformative Research Areas (A) (nos. 20H05867 and 20H05862) from MEXT. J.L. is grateful for the funding from The University of Hong Kong (HKU) and ITC to the SKL. The authors thank the UGC funding administered by HKU for supporting the Time-of-Flight Mass Spectrometry Facilities under the Support for Interdisciplinary Research in Chemical Science. The authors acknowledge the computer cluster (HPC2021) of HKU for generous allocations of compute resources, and Dr. Shugo Sakaguchi at Kyoto University for AFM and XRD measurements.

Conflict of Interest

The authors declare no conflict of interest.

Data Availability Statement

The data that support the findings of this study are available in the supplementary material of this article.

Keywords

boron-nitrogen atoms, delayed fluorescence, nanographenes, pentagon–heptagon rings, polycyclic aromatic hydrocarbons

Received: February 28, 2023
Revised: April 3, 2023
Published online:

[1] a) E. Clar, *Polycyclic Hydrocarbons*, Academic Press, London **1964**; b) E. Clar, *The Aromatic Sextet*, Wiley, London **1972**; c) X. Feng, W. Pisula, K. Müllen, *Pure Appl. Chem.* **2009**, *81*, 2203.

[2] a) A. Narita, X.-Y. Wang, X. Feng, K. Müllen, *Chem. Soc. Rev.* **2015**, *44*, 6616; b) L. Chen, Y. Hernandez, X. Feng, K. Müllen, *Angew. Chem., Int. Ed.* **2012**, *51*, 7640; c) Y. Segawa, H. Ito, K. Itami, *Nat. Rev. Mater.* **2016**, *1*, 15002; d) J. Wu, W. Pisula, K. Müllen, *Chem. Rev.* **2007**, *107*, 718; e) W. Pisula, X. Feng, K. Müllen, *Chem. Mater.* **2011**, *23*, 554; f) J. Liu, X. Feng, *Angew. Chem., Int. Ed.* **2020**, *59*, 23386.

[3] a) L. T. Scott, M. M. Hashemi, D. T. Meyer, H. B. Warren, *J. Am. Chem. Soc.* **1991**, *113*, 7082; b) V. M. Tsefrikas, L. T. Scott, *Chem. Rev.* **2006**, *106*, 4868; c) X. Li, F. Kang, M. Inagaki, *Small* **2016**, *12*, 3206.

[4] a) H. Sakurai, T. Daiko, T. Hirao, *Science* **2003**, *301*, 1878; b) T. Amaya, T. Hirao, *Chem. Rec.* **2015**, *15*, 310.

[5] a) K. Y. Cheung, X. Xu, Q. Miao, *J. Am. Chem. Soc.* **2015**, *137*, 3910; b) Q. Miao, *Chem. Rec.* **2015**, *15*, 1156; c) K. Kawasumi, Q. Zhang, Y. Segawa, L. T. Scott, K. Itami, *Nat. Chem.* **2013**, *5*, 739; d) C. Chaolumen, I. A. Stepek, K. E. Yamada, H. Ito, K. Itami, *Angew. Chem., Int. Ed.* **2021**, *60*, 23508; e) I. R. Márquez, S. Castro-Fernández, A. Millán, A. G. Campaña, *Chem. Commun.* **2018**, *54*, 6705; f) C. M. Cruz, I. R. Marquez, S. Castro-Fernandez, J. M. Cuerva, E. Macos, A. G. Campaña, *Angew. Chem., Int. Ed.* **2019**, *58*, 8068.

[6] a) J. Liu, S. Mishra, C. A. Pignedoli, D. Passerone, J. I. Urgel, A. Fabrizio, T. G. Lohr, J. Ma, H. Komber, M. Baumgarten, C. Corminboeuf, R. Berger, P. Ruffieux, K. Müllen, R. Fasel, X. Feng, *J. Am. Chem. Soc.* **2019**, *141*, 12011; b) J. Ma, Y. Fu, E. Dmitrieva, F. Liu, H. Komber, F. Hennersdorf, A. A. Popov, J. J. Weigand, J. Liu, X. Feng, *Angew. Chem., Int. Ed.* **2020**, *59*, 5637; c) Y. Fei, Y. Fu, X. Bai, L. Du, Z. Li, H. Komber, K.-H. Low, S. Zhou, D. L. Phillips, X. Feng, J. Liu, *J. Am. Chem. Soc.* **2021**, *143*, 2353; d) X. Yang, F. Rominger, M. Mastalerz, *Angew. Chem., Int. Ed.* **2019**, *58*, 17577; e) A. Konishi, K. Horii, D. Shiomi, K. Sato, T. Takui, M. Yasuda, *J. Am. Chem. Soc.* **2019**, *141*, 10165; f) X.-S. Zhang, Y.-Y. Huang, J. Zhang, W. Meng, Q. Peng, R. Kong, Z. Xiao, J. Liu, M. Huang, Y. Yi, L. Chen, Q. Fan, G. Lin, Z. Liu, G. Zhang, L. Jiang, D. Zhang, *Angew. Chem., Int. Ed.* **2020**, *59*, 3529; g) Q. Jiang, T. Tao, H. Phan, Y. Han, T. Y. Gopalakrishna, T. S. Herng, G. Li, L. Yuan, J. Ding, C. Chi, *Angew. Chem., Int. Ed.* **2018**, *57*, 16737; h) Y. Han, Z. Xue, G. Li, Y. Gu, Y. Ni, S. Dong, C. Chi, *Angew. Chem., Int. Ed.* **2020**, *59*, 9026; i) N. Ogawa, Y. Yamaoka, H. Takikawa, K. Yamada, K. Takasu, *J. Am. Chem. Soc.* **2020**, *142*, 13322; j) C. Zhu, K. Shoyama, F. Würthner, *Angew. Chem., Int. Ed.* **2020**, *59*, 21505; k) B. Pigulski, K. Shoyama, F. Würthner, *Angew. Chem., Int. Ed.* **2020**, *59*, 15908; l) H. Xin, X. Gao, *ChemPlusChem* **2017**, *82*, 945; m) A. Konishi, M. Yasuda, *Chem. Lett.* **2021**, *50*, 195.

[7] M. Stępień, E. Gońka, M. Żyła, N. Sprutta, *Chem. Rev.* **2017**, *117*, 3479.

[8] S. K. Mellerup, S. Wang, *Trends Chem.* **2019**, *1*, 77.

[9] X.-Y. Wang, J.-Y. Wang, J. Pei, *Chem. - Eur. J.* **2015**, *21*, 3528.

[10] a) M. J. D. Bosdet, W. E. Piers, T. S. Sorensen, M. Parvez, *Angew. Chem., Int. Ed.* **2007**, *46*, 4940; b) T. Hatakeyama, S. Hashimoto, S. Seki, M. Nakamura, *J. Am. Chem. Soc.* **2011**, *133*, 18614; c) X.-Y. Wang, F.-D. Zhuang, R.-B. Wang, X.-C. Wang, X.-Y. Cao, J.-Y. Wang, J. Pei, *J. Am. Chem. Soc.* **2014**, *136*, 3764; d) S. Wang, D.-T. Yang, J. Lu, H. Shimogawa, S. Gong, X. Wang, S. K. Mellerup, A. Wakamiya, Y.-L. Chang, C. Yang, Z.-H. Lu, *Angew. Chem., Int. Ed.* **2015**, *54*, 15074; e) P. B. Pati, E. Jin, Y. Kim, Y. Kim, J. Mun, S. J. Kim, S. J. Kang, W. Choe, G. Lee, H.-J. Shin, Y. S. Park, *Angew. Chem., Int. Ed.* **2020**, *59*, 14891.

[11] a) S. Ito, Y. Tokimaru, K. Nozaki, *Angew. Chem., Int. Ed.* **2015**, *54*, 7256; b) H. Yokoi, Y. Hiraoka, S. Hiroto, D. Sakamaki, S. Seki, H. Shinokubo, *Nat. Commun.* **2015**, *6*, 8215; c) S. Higashibayashi, P. Pandit, R. Haruki, S. Adachi, R. Kumai, *Angew. Chem., Int. Ed.* **2016**, *55*, 10830; d) S. Nakatsuka, N. Yasuda, T. Hatakeyama, *J. Am. Chem. Soc.* **2018**, *140*, 13562; e) M. Krzeszewski, Ł. Dobrzycki, A. L. Sobolewski, M. K. Cyranski, D. T. Gryko, *Angew. Chem., Int. Ed.* **2021**, *60*, 14998.

[12] a) X. Wang, F. Zhang, J. Liu, R. Tang, Y. Fu, D. Wu, Q. Xu, X. Zhuang, G. He, X. Feng, *Org. Lett.* **2013**, *15*, 5714; b) W. Zhang, F. Zhang, R. Tang, Y. Fu, X. Wang, X. Zhuang, G. He, X. Feng,

Org. Lett. **2016**, *18*, 3618; c) Y. D-T, T. Nakamura, Z. He, X. Wang, A. Wakamiya, T. Peng, S. Wang, *Org. Lett.* **2018**, *20*, 6741.
[13] Y. Wan, A. Stradomska, J. Knoester, L. Huang, *J. Am. Chem. Soc.* **2017**, *139*, 7287.
[14] K. T. Chan, G. S. M. Tong, W.-P. To, C. Yang, L. Du, D. L. Phillips, C.-M. Che, *Chem. Sci.* **2017**, *8*, 2352.
[15] T. N. Singh-Rachford, F. N. Castellano, *Coord. Chem. Rev.* **2010**, *254*, 2560.
[16] a) S. Seki, A. Saeki, T. Sakurai, D. Sakamaki, *Phys. Chem. Chem. Phys.* **2014**, *16*, 11093; b) H. Abe, A. Kawasaki, T. Takeda, N. Hoshino, S. Seki, T. Akutagawa, *J. Am. Chem. Soc.* **2021**, *143*, 1046.
[17] a) Y. Honsho, T. Miyakai, T. Sakurai, A. Saeki, S. Seki, *Sci. Rep.* **2013**, *3*, 3182; b) Y. Tsutsui, G. Schweicher, B. Chattopadhyay, T. Sakurai, J.-B. Arlin, C. Ruzié, A. Aliev, A. Ciesielski, S. Colella, A. R. Kennedy, V. Lemaur, Y. Olivier, R. Hadji, L. Sanguinet, F. Castet, D. Beljonne, J. Cornil, P. Samorì, S. Seki, Y. H. Geerts, *Adv. Mater.* **2016**, *28*, 7106; c) F. Zhang, V. Lemaur, W. Choi, P. Kafle, S. Seki, J. Cornil, D. Beljonne, Y. Diao, *Nat. Commun.* **2019**, *10*, 4217.